

See discussions, stats, and author profiles for this publication at: <https://www.researchgate.net/publication/270902026>

# Nanoepitaxy of Anatase-type TiO<sub>2</sub> on CeO<sub>2</sub> Nanocubes Self-Assembled on a Si Substrate for Fabricating Well-Aligned Nanoscale Heterogeneous Interfaces

ARTICLE *in* CRYSTAL GROWTH & DESIGN · AUGUST 2014

Impact Factor: 4.89 · DOI: 10.1021/cg500821z

---

READS

29

## 10 AUTHORS, INCLUDING:



Daisuke Hojo

Tohoku University

53 PUBLICATIONS 313 CITATIONS

[SEE PROFILE](#)



Takanari Togashi

Tohoku University

31 PUBLICATIONS 139 CITATIONS

[SEE PROFILE](#)



Yuichi Ikuhara

The University of Tokyo

478 PUBLICATIONS 5,914 CITATIONS

[SEE PROFILE](#)



Taro Hitosugi

Tohoku University

144 PUBLICATIONS 1,949 CITATIONS

[SEE PROFILE](#)

# Nanoepitaxy of Anatase-type $\text{TiO}_2$ on $\text{CeO}_2$ Nanocubes Self-Assembled on a Si Substrate for Fabricating Well-Aligned Nanoscale Heterogeneous Interfaces

Daisuke Hojo,<sup>\*,†</sup> Takanari Togashi,<sup>§</sup> Takeo Ohsawa,<sup>‡</sup> Mitsuhiro Saito,<sup>†</sup> Zhongchang Wang,<sup>†</sup> Yusuke Sakuda,<sup>||</sup> Shunsuke Asahina,<sup>||</sup> Yuichi Ikuhara,<sup>†,‡</sup> Taro Hitosugi,<sup>†</sup> and Tadafumi Adschiri<sup>\*,†,‡</sup>

<sup>†</sup>Advanced Institute for Materials Research, Tohoku University, Katahira 2-1-1 Aoba-ku, Sendai 980-8577, Japan

<sup>‡</sup>National Institute for Materials Science, 1-1 Namiki, Tsukuba 305-0044, Japan

<sup>§</sup>Department of Material and Biological Chemistry, School of Engineering, Yamagata University, 1-4-12 Kojirakawa-machi, Yamagata 990-8560, Japan

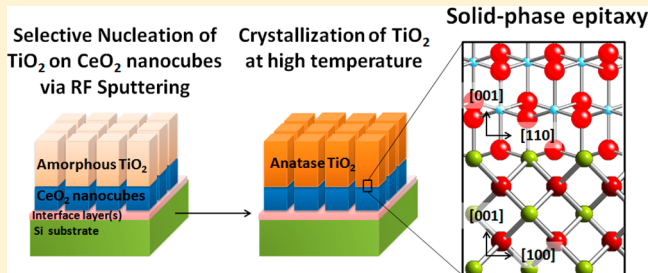
<sup>||</sup>JEOL Ltd., 1-2 Musashino 3-chome, Akishima 196-8558, Japan

<sup>†</sup>Institute of Engineering Innovation, School of Engineering, The University of Tokyo, 7-3-1 Hongo, Bunkyo-ku, Tokyo 113-8656, Japan

<sup>#</sup>Institute of Multidisciplinary Research for Advanced Materials, Tohoku University, Katahira 2-1-1 Aoba-ku, Sendai 980-8577, Japan

## S Supporting Information

**ABSTRACT:** Nanoscale epitaxy or nanoepitaxy for fabricating macroscopically well-aligned nanoscale heterogeneous interfaces on a Si substrate is demonstrated, combining bottom-up and top-down processes efficiently.  $\text{TiO}_2$  sputtered in vacuum was selectively nucleated on the atomically flat surfaces of individual  $\text{CeO}_2$  nanocubes prefabricated by self-assembly in solution on the substrate, and anatase-type  $\text{TiO}_2$  was grown after a heat treatment by solid-phase epitaxy to produce tandem nanocrystals with heterogeneous interfaces. The atomic configurations of the tandem nanocrystals fabricated after sputtering and subsequent annealing were determined using high-resolution scanning transmission electron microscopy to characterize the nanoscale heterogeneous interfaces. Sharp heterogeneous interfaces were observed between the anatase  $\text{TiO}_2$ (001) and the  $\text{CeO}_2$ (001) nanocubes, with the  $\text{TiO}_2$  [110] directions being parallel to the  $\text{CeO}_2$  [100] directions. This unique nanoepitaxial growth technique will contribute to the development of devices and catalytic materials incorporating functional tandem nanocrystals with nanoscale heterogeneous interfaces.



## INTRODUCTION

Heterogeneous interfaces are of particular importance from the viewpoint of both science and technology because of the unique phenomena associated with them.<sup>1–3</sup> Of late, nanoscale heterogeneous interfaces are attracting a lot of interest. This is because many unique phenomena, including those related to plasmonic,<sup>4–7</sup> electronic,<sup>8–17</sup> and magnetic characteristics,<sup>18–20</sup> as well as those that enhance catalytic effects,<sup>21–27</sup> originate from the heterogeneity at these interfaces. Given the confinement of charge carriers along the in-plane directions of nanoscale interfaces as well as the direction perpendicular to the interfaces, it is believed that such interfaces ought to exhibit unique characteristics related to quantum confinement effects.<sup>28,29</sup> Therefore, the electrical, optical, and magnetic characteristics of nanometer-sized materials with nanoscale heterogeneity, including those with nanoscale surfaces, are expected to be different from those of the respective bulk materials.<sup>30</sup> Furthermore, by designing nanoscale heterogeneity through the fabrication of nanoscale heterogeneous interfaces,

it should be possible to achieve and manipulate desirable macroscopic functionalities.

Three methods for fabricating nanoscale interfaces have been reported so far. The first involves the synthesis of tandem or core/shell nanocrystals in solution<sup>5–7,10,11,13,17–20,22,24,31–41</sup> or in a gas phase.<sup>12,14,26,27,42</sup> This process exploits the heterogeneous nucleation that occurs on the surfaces of the host nanocrystals or nanorods. Ibáñez et al. investigated the thermoelectric properties of a PbTe–PbS core/shell nanocomposite, which was fabricated by the epitaxial growth of PbTe on PbS nanocrystals in solution.<sup>17</sup> Wang et al. reported the heterogeneous nucleation of bimetallic nanocrystals in the liquid phase, wherein alloyed structures of the bimetallic nanocrystals were synthesized along with tandem or core/shell nanostructures.<sup>38</sup> The second method involves the fabrication

Received: June 5, 2014

Revised: July 29, 2014

Published: August 1, 2014



**Scheme 1.** (a) Uniform  $\text{CeO}_2$  Nanocrystalline Monolayer Fabricated on a Modified Si Substrate. (b) Sputtering of  $\text{TiO}_2$  on the Nanocrystalline Monolayer for the Selective Nucleation of  $\text{TiO}_2$ . (c) Crystallization of  $\text{TiO}_2$  Nucleated on Each of the  $\text{CeO}_2$  Nanocrystals Heat-Treated at 400°C

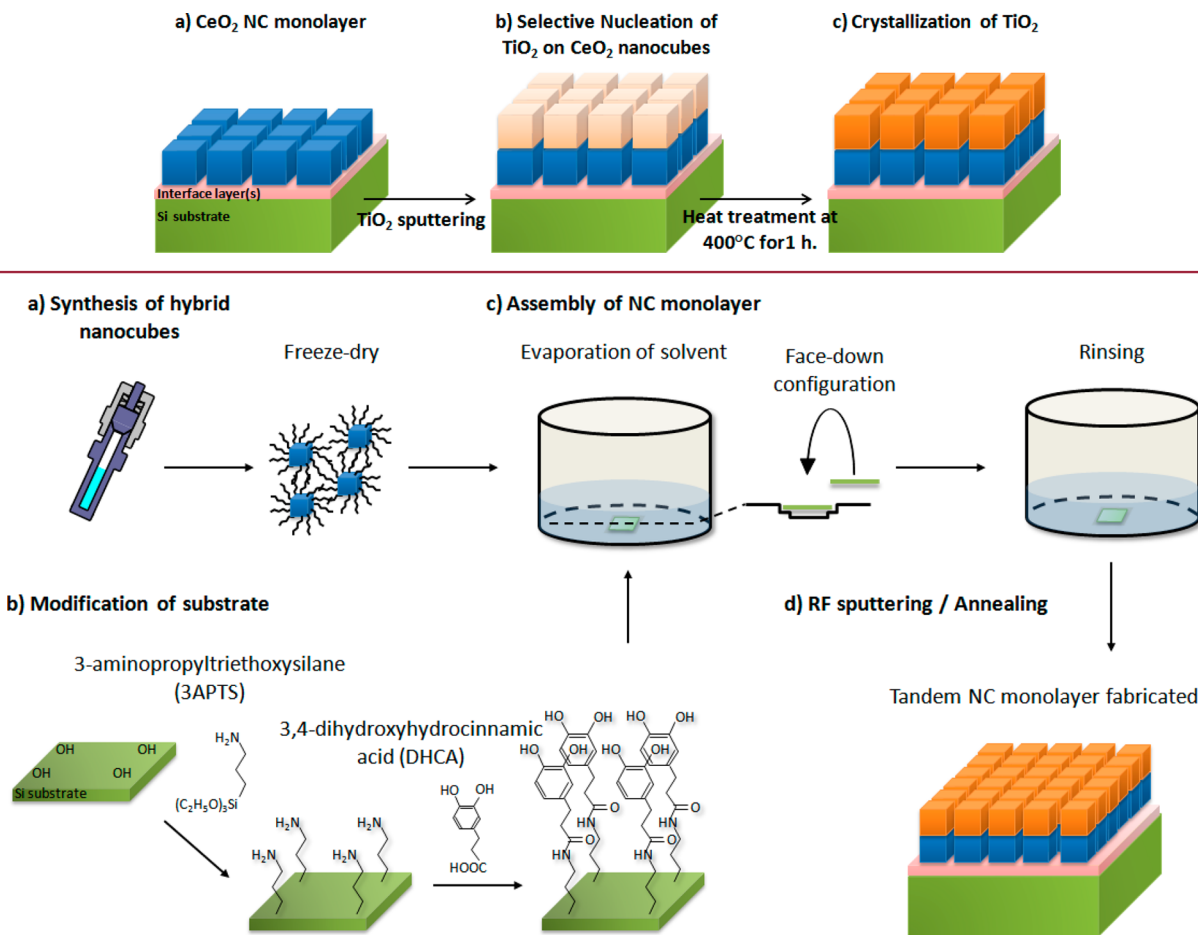


**Figure 1.** (a) Synthesis of decanoic acid modified  $\text{CeO}_2$  nanocrystals in supercritical water. (b) Modification of silicon substrate to establish chemisorption between the nanocrystals and the substrate. (c) Self-assembly of nanocrystals and rinsing to assemble nanocrystalline (NC) monolayer. (d) RF sputtering of  $\text{TiO}_2$  and subsequent annealing to fabricate tandem nanocrystals of  $\text{CeO}_2$  and  $\text{TiO}_2$  on the substrate.

of nanocomposites using organic linkers; this process is based on the nanoscale interfaces formed between organic and inorganic materials.<sup>8,9,16,25</sup> Miljevic et al. used bifunctional linkers to bridge Au and  $\text{TiO}_2$  nanocrystals in order to improve their photocatalytic activity.<sup>25</sup> Hamed et al. also used a conducting polymer as a linker between Au nanocrystals to establish organic and inorganic conducting interfaces.<sup>9</sup> Finally, the third method is the layer-by-layer assembly of two different kinds of nanocrystals on a substrate.<sup>15,21</sup> Yamada et al. reported that  $\text{CeO}_2$  nanocrystals could be deposited on Pt nanocrystals prefabricated on a substrate to produce nanoscale heterogeneous interfaces that improved catalytic activity.<sup>21</sup> MacDonald et al. reported the layer-by-layer assembly of CdSe and CdTe nanocrystals for use in solar cells.<sup>15</sup> The alignment of the nanocrystals on the substrate is of critical importance and difficult to achieve. For instance, it is difficult to align nanocrystals in a tandem manner along the desired direction using the first and second methods. Likewise, it is extremely difficult to position nanocrystals on top of other nanocrystals in a one-on-one fashion to fabricate nanoscale interfaces using the third method. Thus, an effective technique for aligning nanoscale interfaces macroscopically needs to be developed for realizing functional materials with nanoscale heterogeneity.

In this study, we grew  $\text{TiO}_2$  through solid-phase epitaxy on individual cubic  $\text{CeO}_2$  nanocrystals (or nanocubes) that were prealigned through self-assembly on a substrate. To fabricate the tandem nanocrystals with nanoscale heterogeneous interfaces, we combined a top-down vacuum-based process with a bottom-up solution-based one. Bottom-up processes are generally used to fabricate well-aligned nanoscale heterogeneous interfaces on substrates.<sup>15,21</sup> Recently, we had reported a simple and efficient method for self-assembling  $\text{CeO}_2$  nanocubes ( $\sim 6 \text{ nm}$ ) on modified surfaces (see Scheme 1a).<sup>43,44</sup> A high-coverage, uniform nanocrystalline monolayer could be fabricated on the substrate surface over a macroscopic area using this method. Exploiting these advantages, in this study,  $\text{TiO}_2$  was sputtered on a monolayer of  $\text{CeO}_2$  nanocubes that was used as a nanoscale substrate to produce tandem nanocrystals (Scheme 1b). Then, crystals of  $\text{TiO}_2$  were made to nucleate on each  $\text{CeO}_2$  nanocube by heating the substrate in a furnace at 400 °C for 1 h in an argon environment,<sup>45</sup> yielding well-aligned heterogeneous interfaces by solid-phase epitaxy (Scheme 1c).

## ■ RESULTS AND DISCUSSION

The experimental procedures can be described in brief as follows; additional details are available in the Experimental Section. Decanoic acid modified  $\text{CeO}_2$  nanocubes were synthesized under hydrothermal conditions<sup>46</sup> (Figure 1a). The silicon substrate used was modified so that the catechol group of 3,4-dihydroxyhydrocinnamic acid (DHCA) could coordinate with the solid surfaces of the nanocubes in exchange with the carboxyl group of decanoic acid at the interfaces between the nanocubes and the DHCA layers<sup>43,44</sup> (Figure 1b). This contributed to the formation of chemical bonds between the nanocubes and the substrate. As a result, the nanocube monolayer remained on the substrate even after washing. The process for modifying the substrate in order to fabricate the nanocrystalline monolayer has been discussed in detail elsewhere.<sup>43</sup> A  $\text{CeO}_2$  nanocrystalline monolayer was successfully fabricated from the solution in which the nanocubes were dispersed (initially 0.5 wt %) in the face-down configuration; the solvent that remained in the hollow beneath the substrate was used for the assembly, as illustrated in Figure 1c.<sup>44</sup> Next, the substrate was rinsed with cyclohexane, in keeping with a previously reported procedure<sup>43,44</sup> (Figure 1c). Finally, after the radio frequency (RF) sputtering of  $\text{TiO}_2$  on the nanocrystalline monolayer, tandem nanoparticles of  $\text{CeO}_2$  and  $\text{TiO}_2$  could be obtained (Figure 1d). The structures of the tandem nanoparticles were observed before crystallization using field-emission scanning electron microscopy (FESEM) (JSM-7800F, JEOL). After annealing at 400 °C to allow for crystallization to occur, the fabricated tandem nanocrystallites were characterized using high-resolution transmission electron microscopy (HRTEM) (JEM-2100F, JEOL), scanning transmission electron microscopy (STEM) (JEM-ARM200F, JEOL), grazing-incident small-angle X-ray scattering (GISAXS) Nanoviewer, Rigaku), and X-ray diffraction (XRD) analyses (SmartLab, Rigaku).

The SEM image in Figure 2a shows that a high-coverage nanocrystalline monolayer of  $\text{CeO}_2$  was adsorbed onto the substrate and remained there even after subsequent rinsing. The cubic nanocrystals of  $\text{CeO}_2$  can be clearly seen in the image. The size of the nanocubes obtained from this image was  $5.94 \pm 0.78$  nm. The nanocubes on the nanocrystalline

monolayer were washed away, leaving behind the monolayer on the modified surface in the areas where there was selective adhesion between the nanocubes and the substrate; this process has been described in detail elsewhere.<sup>43</sup> The nanocubes that remained on the nanocrystalline monolayer appear as white spots in the SEM image. GISAXS analysis confirmed that the nanocrystalline monolayer was formed macroscopically on the substrate, as the peak associated with the distance between the adsorbed nanocubes was clearly visible. This point is described in detail in the Supporting Information.

After the sputtering process,  $\text{TiO}_2$  nanocrystals nucleated selectively in a one-on-one fashion and grew on each of the  $\text{CeO}_2$  nanocubes. As a result, tandem nanoparticles of  $\text{CeO}_2$  and  $\text{TiO}_2$  could be obtained. The modifiers that had been attached to the nanocubes seemed to have burnt away, owing to the plasma treatment during the sputtering process. The SEM image in Figure 2b shows the nanocrystalline monolayer after the sputtering-based deposition of  $\text{TiO}_2$  for 80 s; the image was obtained before the heat treatment. The edges of each of the tandem nanoparticles became blurred, in contrast to what was noticed before deposition. The atoms of cerium, which are heavier, reflect a greater number of secondary electrons than do those of titanium and silicon, resulting in clearer images, as can be seen from Figure 2a. The grain size appeared to be slightly larger in the SEM image obtained after deposition. The size had increased to  $6.20 \pm 0.97$  nm owing to the deposition of  $\text{TiO}_2$ . This indicates that  $\text{TiO}_2$  nucleated selectively on each of the  $\text{CeO}_2$  nanocubes in a one-on-one fashion, producing the tandem structures. Panels (c) and (d) in Figure 2 show images of the tandem nanoparticles after  $\text{TiO}_2$  deposition for 200 and 400 s, respectively. With the increase in the sputtering time, the nanoparticle shape transformed from cubic to polyhedral. This result also suggested that selective nucleation occurred on each of the  $\text{CeO}_2$  nanocubes. The size of the nanoparticles increased further to  $6.55 \pm 1.02$  and  $6.96 \pm 1.30$  nm after deposition for 200 and 400 s, respectively. However, the boundary of each nanoparticle could still be seen in the images even after deposition for 400 s. In particular, the deposition of  $\text{TiO}_2$  on the  $\text{CeO}_2$  nanocubes that remained on the nanocrystalline monolayer was more efficient compared to growth in the monolayer, because there was more space to grow laterally. This contributed to the increase in the size of the nanocubes after the deposition of  $\text{TiO}_2$ . That this phenomenon occurred was also proven macroscopically using GISAXS analysis. As the sputtering time was increased, the peak positions shifted to the right, suggesting that the distance between individual nanoparticles apparently became smaller. Further, the peak heights decreased owing to the increase in the size distribution. This is described in detail in the Supporting Information.

Cross-sectional STEM images confirmed that the tandem nanocrystalline structure consisting of  $\text{CeO}_2$  nanocrystals and  $\text{TiO}_2$  layers remained intact even after the subsequent heat treatment or crystallization. The high-angle annular dark field (HAADF)-STEM images in Figure 3a,b show that the  $\text{TiO}_2$  layer was sputtered uniformly on the  $\text{CeO}_2$  nanocrystalline monolayer; the images show  $\text{TiO}_2$  layers grown for sputtering times of 200 and 400 s, respectively. The  $\text{CeO}_2$  nanocubes in the nanocrystalline monolayer appear bright white because their constituent atoms are heavier than are those of titanium and silicon, while the  $\text{TiO}_2$  layer grown on the nanocrystalline monolayer appears gray in the HAADF images. A few of the  $\text{CeO}_2$  nanocubes appear to be rectangular in the images; this

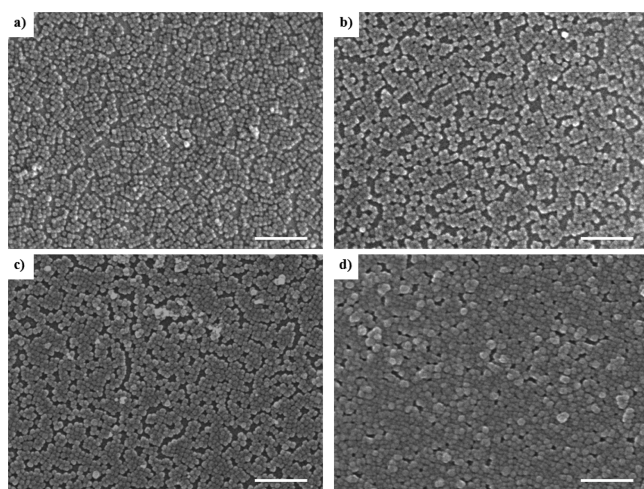


**Figure 2.** SEM images of (a) the  $\text{CeO}_2$  nanocrystalline monolayer before the deposition of  $\text{TiO}_2$  and after deposition for sputtering times of (b) 80, (b) 200, and (c) 400 s. Scale bars = 80 nm.

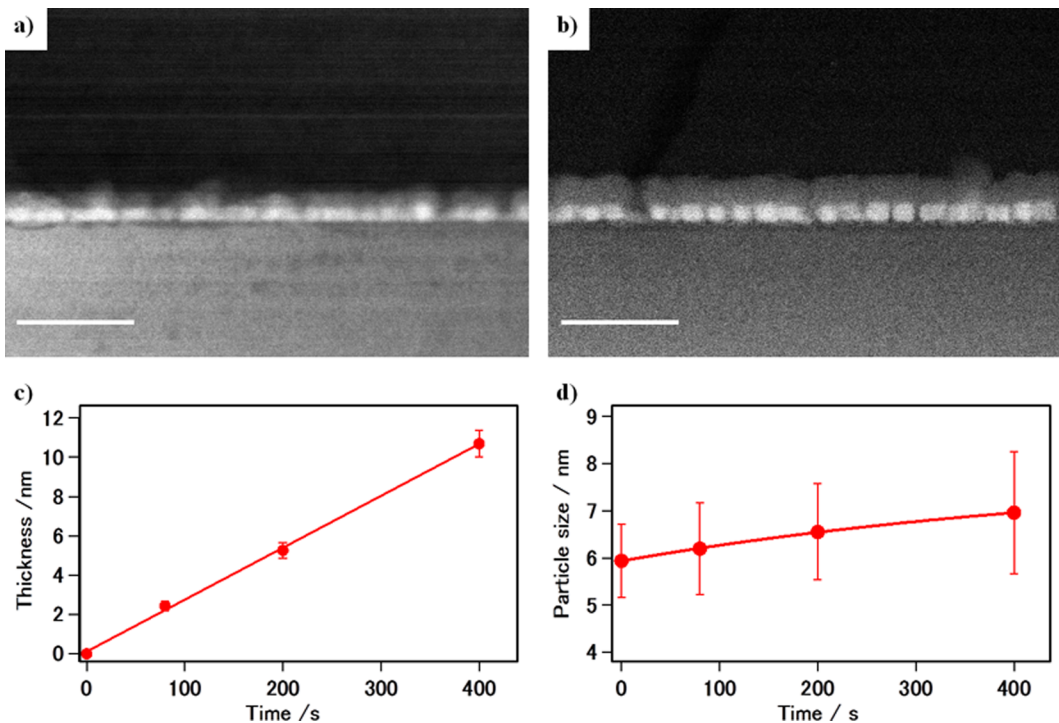


**Figure 3.** HAADF-STEM images of tandem nanocrystals of  $\text{CeO}_2$  and  $\text{TiO}_2$  fabricated by sputtering  $\text{TiO}_2$  for (a) 200 and (b) 400 s. (c) The thickness of the deposited  $\text{TiO}_2$  layer is plotted as a function of the deposition time. (d) The particle size after the deposition of  $\text{TiO}_2$  is plotted as a function of the deposition time. Scale bars in (a) and (b) = 50 nm.

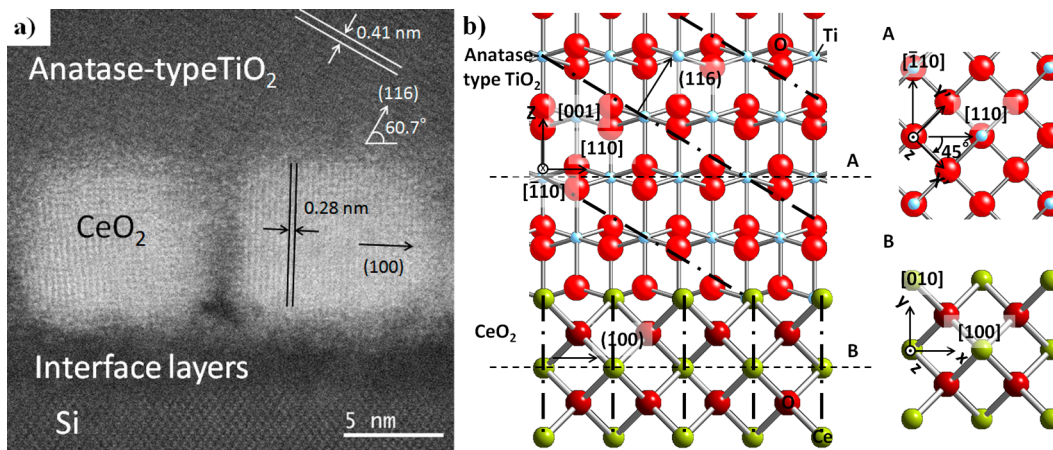


**Figure 4.** (a) HAADF-STEM image of tandem nanocrystals of  $\text{CeO}_2$  and  $\text{TiO}_2$ . The thickness of the  $\text{TiO}_2$  layer in the sample is 10.7 nm. (b) Schematic of tandem nanocrystals of  $\text{CeO}_2$  and  $\text{TiO}_2$ . The atomic structures at the cross sections of lines A and B are also illustrated.

means that these nanocubes were deposited at a certain angle to the cross-sectional plane. The distinctive mushroom-like shape of the  $\text{TiO}_2$  nanocrystals grown on each  $\text{CeO}_2$  nanocube is attributable to the selective nucleation process and the nature of the crystalline growth of the nanocrystals; these are described in the next section. The thicknesses of the  $\text{TiO}_2$  crystalline layers grown on the nanocubes were evaluated using the HRTEM and STEM images and were found to increase monotonically with the sputtering time, as shown in Figure 3c. The growth rate of  $\text{TiO}_2$  on the nanocubes was determined to be 0.026 nm/s, which was comparable to the growth rate (0.025 nm/s) when  $\text{TiO}_2$  was deposited on a Si substrate during preliminary experiments. Further, in Figure 3d, the particle size, determined from the SEM images, is plotted as a function of the sputtering time. The particle size plateaued as

the sputtering time was increased, and the size distribution increased as discussed in the previous section. It appears that the lateral growth of the  $\text{TiO}_2$  nanocrystals was suppressed, in contrast to their longitudinal growth on the  $\text{CeO}_2$  nanocubes.

This constrained growth in the lateral direction was not only because the aligned nanocrystals interfere with one another but also because of the nature of the crystalline growth of anatase-type  $\text{TiO}_2$ , which nucleated on the  $\text{CeO}_2$  nanocubes. A high-resolution HAADF-STEM image of the tandem nanocrystals is shown in Figure 4a. The thickness of the  $\text{TiO}_2$  layer in this sample was 10.7 nm. That anatase  $\text{TiO}_2$  was grown on the  $\text{CeO}_2$  nanocrystalline monolayer was confirmed through XRD analyses, which are discussed in detail in the Supporting Information. Further, it was also confirmed that anatase  $\text{TiO}_2$  was grown on each  $\text{CeO}_2$  nanocube because uniform single-

crystalline  $\text{TiO}_2$  structures can be seen on each  $\text{CeO}_2$  nanocube in the HAADF image in Figure 4a. The lattice fringes of the  $\text{TiO}_2$  layers are clearly visible in the image. The titanium atoms are aligned at an angle of  $60.7^\circ$  with respect to the plane perpendicular to the Si substrate. This angle is similar to the angle ( $59.35^\circ$ ) between the [110] and [116] directions in anatase  $\text{TiO}_2$ , when viewed from the [110] direction. The spacing between these titanium lines was  $0.41\text{ nm}$  on average; this value is 3 times the distance between the {116} facets of anatase  $\text{TiO}_2$ . The lattice constants  $a$  and  $c$  of this tetragonal phase are  $0.379$  and  $0.951\text{ nm}$ , respectively (JCPDS No. 21-1272). Therefore, it was confirmed that anatase  $\text{TiO}_2$  grew toward the [001] direction on each of the  $\text{CeO}_2$  nanocubes, as shown schematically in Figure 4b.

A sharp interface was formed between the  $\text{TiO}_2$  and  $\text{CeO}_2$  nanocrystals, as shown in Figure 4a. To characterize this complex interface, the crystalline structure of the aligned  $\text{CeO}_2$  nanocubes was also investigated. The HAADF STEM image in Figure 4a shows clearly the cerium atomic columns in the  $\text{CeO}_2$  nanocubes. The distance between the lattices appears to be  $0.28\text{ nm}$ ; this value corresponds to the space between the {100} facets of  $\text{CeO}_2$ , which has a fluorite-like structure with a lattice constant of  $0.5412\text{ nm}$  (JCPDS No. 81-0792). The cubic  $\text{CeO}_2$  nanocrystals were well-aligned in that the (001) surfaces of the nanocubes were attached to the silicon substrate. Further, three-dimensional HRTEM images had shown that the surfaces of the  $\text{CeO}_2$  nanocubes were atomically flat; the exception was their corners.<sup>47</sup> Thus, anatase  $\text{TiO}_2$  was epitaxially grown along the [001] direction on the (001) surfaces of the  $\text{CeO}_2$  nanocubes with an in-plane rotation of  $45^\circ$ , as shown in Figure 4b. That this epitaxial relationship existed is further supported by the relationships noticed during other studies on epitaxial thin-film growth. It is known that anatase  $\text{TiO}_2$ (001) thin films can be grown epitaxially on  $\text{LaAlO}_3$ (001) substrates.<sup>48</sup> Further, it has been reported that  $\text{CeO}_2$ (001) can be grown epitaxially on  $\text{LaAlO}_3$ (001) substrates with a  $45^\circ$  rotation.<sup>49</sup> These results strongly suggest that anatase  $\text{TiO}_2$ (001) grows on  $\text{CeO}_2$ (001) with a  $45^\circ$  rotation owing to the small lattice misfit between the  $\text{CeO}_2$  {100} facets and the anatase  $\text{TiO}_2$  {110} facets ( $\sim 1.1\%$ ). Hence, the result that anatase-type  $\text{TiO}_2$  and not rutile-type  $\text{TiO}_2$  grew dominantly on the  $\text{CeO}_2$  nanocubes is consistent with fact that only a small percentage of the  $\text{CeO}_2$  {111} facets and {011} facets were exposed to the surfaces of the  $\text{CeO}_2$  nanocubes, where the  $\text{CeO}_2$  {100} facets are dominant.<sup>46,47</sup>

## CONCLUSIONS

In summary, sputtered anatase-type  $\text{TiO}_2$  could be selectively nucleated in a one-on-one fashion and grown epitaxially after a heat treatment on a nanocrystalline monolayer of  $\text{CeO}_2$  that was self-assembled macroscopically on a Si substrate, yielding well-aligned nanoscale heterogeneous interfaces. High-resolution HAADF STEM images revealed that the anatase  $\text{TiO}_2$  grew uniformly along the [001] direction on the (001) surfaces of each of the  $\text{CeO}_2$  nanocubes such that the anatase  $\text{TiO}_2$  [110] directions were parallel to the  $\text{CeO}_2$  [100] directions at the nanoscale heterogeneous interface. The growth rate of  $\text{TiO}_2$  on the  $\text{CeO}_2$  nanocubes was determined to be  $0.026\text{ nm/s}$ ; this was comparable to that on a silicon surface. The size of the tandem nanocrystals reached a maximum as the sputtering time was increased. The growth of the  $\text{TiO}_2$  nanocrystals was found to be constrained in the lateral direction, owing to the fact that anatase  $\text{TiO}_2$  grows in the [001] direction.

## EXPERIMENTAL SECTION

**Preparation of Decanoic Acid Modified Cubic  $\text{CeO}_2$  Nanocrystals.** The precursor  $0.1\text{ M}$  hydroxylated cerium oxide and  $2.5\text{ mL}$  of water were placed in a pressure-resistant Hastelloy vessel (inner volume =  $5\text{ mL}$ ). Next,  $0.13\text{ mg}$  of decanoic acid, used as a modifier, was placed in the vessel. As a pretreatment, the mixture was heated at  $150^\circ\text{C}$  for  $20\text{ min}$  with a Hastelloy sphere. This resulted in a well-mixed solution of the precursor and modifier. Next, the hydrothermal reaction was made to occur in the reactor at  $400^\circ\text{C}$  for  $10\text{ min}$ . The organic-ligand-modified nanocubes were extracted from the product mixture using hexane ( $5\text{ mL}$ ) after removing the water phase. The products were precipitated from the resulting hexane phase using ethanol ( $3.75\text{ mL}$ ) as an antisolvent agent and were separated using centrifugation. The centrifuged products were then washed twice with a mixture of toluene ( $1.25\text{ mL}$ ) and ethanol ( $7.5\text{ mL}$ ). The washed products were dissolved in cyclohexane ( $5\text{ mL}$ ), which was then freeze-dried to obtain the final products, as illustrated in Figure 1a.

**Modification of Silicon Substrate to Fabricate  $\text{CeO}_2$  Nanocrystalline Monolayer.** Silicon (100) substrates with dimensions of  $0.8\text{ cm} \times 0.8\text{ cm}$  were subjected to an ozone treatment for  $30\text{ min}$  to produce hydroxylated silicon oxide on their surfaces. To create adsorption sites for the modified  $\text{CeO}_2$  nanocubes, first,  $1.15\text{ g}$  of 3-aminopropyltriethoxysilane (3APTS) was added to a mixture of ethanol ( $45.6\text{ mL}$ ), water ( $0.76\text{ mL}$ ), and  $28\%$  ammonium hydroxide ( $1.26\text{ mL}$ ). Each substrate was dipped into this solution for  $5\text{--}6\text{ h}$  to produce terminated amine groups. Next, the substrate was rinsed with ethanol to remove any unmodified 3APTS. Then, the substrate was heated at  $130^\circ\text{C}$  for  $2\text{ h}$  in order to attach the 3APTS firmly to it. The substrate was then immersed in  $5\text{ mL}$  of  $N,N$ -dimethylformamide (DMF) containing  $0.2\text{ M}$  of 3,4-dihydroxyhydrocinnamic acid (DHCA),  $0.2\text{ M}$  of 1-ethyl-3-(3-(dimethylamino)propyl) carbodiimide hydrochloride (a condensation agent), and  $0.02\text{ M}$  of  $N,N$ -dimethyl-4-aminopyridine (a catalyst) for  $15\text{ h}$ . This caused the condensation of the carboxyl group of DHCA with the amine groups terminated on the substrate, as illustrated in Figure 1b. Finally, the silicon substrate was washed with fresh ethanol to remove any remaining DMF and other chemicals.

**Assembly of  $\text{CeO}_2$  Nanocrystalline Monolayer.** To allow for the adsorption of the  $\text{CeO}_2$  nanocubes on the treated silicon substrate, the substrate was immersed in  $400\text{ mg}$  of cyclohexane containing  $2\text{ mg}$  of the freeze-dried decanoic acid modified  $\text{CeO}_2$  cubic nanocrystals or nanocubes. The solvent was then gradually evaporated at a pressure of  $300\text{ hPa}$ ; the pressure was regulated using an evaporator (Vacuum Controller V-850, BUCHI). The face-down configuration, in which the solvent remains in a hollow beneath the substrate, was used for the self-assembly of the nanocubes. After the adsorption of the nanocubes, the substrate was rinsed with cyclohexane several times, yielding the nanocrystalline monolayer, as illustrated in Figure 1c.

**Sputtering and Crystallization of  $\text{TiO}_2$  on the  $\text{CeO}_2$  Nanocrystalline Monolayer to Produce Tandem Nanocrystals with Nanoscale Heterogeneous Interfaces.** To deposit  $\text{TiO}_2$  on the  $\text{CeO}_2$  nanocrystalline monolayer in order to fabricate tandem nanocrystals, RF sputtering was performed using a  $\text{TiO}_2$  target in an argon ambient at room temperature in the absence of oxygen. The argon flow was regulated to be  $10\text{ sccm}$  using a mass flow controller. The ambient pressure was  $1\text{ Pa}$ , and the power applied was  $100\text{ W}$ . Through preliminary experiments, the growth rate was determined to be  $0.025\text{ nm/s}$ . Hence, the sputtering durations for  $\text{TiO}_2$  layer thicknesses of  $2$ ,  $5$ , and  $10\text{ nm}$  were  $80$ ,  $200$ , and  $400\text{ s}$ , respectively. The crystallization of  $\text{TiO}_2$  was performed in a tubular furnace at  $400^\circ\text{C}$  for  $1\text{ h}$  in an argon environment; the ambient pressure was  $\sim 100\text{ Pa}$ .

**Characterization of Tandem Nanocrystals of  $\text{TiO}_2$  and  $\text{CeO}_2$ .** High-resolution images of the fabricated structures before the crystallization process were obtained using FESEM (JSM-7800F, JEOL) at an acceleration voltage of  $17\text{ kV}$ . A bias voltage of  $-2\text{ kV}$  was also applied to the samples. To observe the cross sections of the tandem structures after crystallization and to characterize the arrangements of atoms in the  $\text{TiO}_2$  and  $\text{CeO}_2$  crystals, HAADF images were obtained at  $200\text{ kV}$  using a STEM system (JEM-

ARM200F, JEOL) equipped with a probe corrector (CEOS, GmbH). HRTEM and energy-dispersive X-ray spectroscopy (EDX) (JEM-2100F, JEOL) were used to measure the sizes of the CeO<sub>2</sub> nanocubes and the thicknesses of the TiO<sub>2</sub> layers deposited; the acceleration voltage was 200 kV. The samples for these imaging techniques were prepared as follows. First, the substrate was cut into pieces with thicknesses of 1–2 mm. These pieces were stuck together face to face. The slices were then mechanically ground to a thickness of 0.1 mm and further dimpled down to 20 μm. To make the dimpled slices transparent to electrons, the slices were thinned using an argon ion milling apparatus (PIPS691, Gatan) at an acceleration voltage of 4 kV and an irradiation angle of 4°. To macroscopically analyze the fabricated structure before and after TiO<sub>2</sub> sputtering, GISAXS (Nanoviewer, Rigaku) analyses were employed. The X-ray source emitted Cu Kα radiation ( $\lambda = 0.15418 \text{ nm}$ ). The detector used was a PILATUS detector, and the incident angle was 0.1°. For characterizing the crystallinity of the structures, XRD analyses (SmartLab, Rigaku) were performed. The 2θ scans were performed in the grazing-incident mode, with the incident angle being constant at 0.5°.

## ASSOCIATED CONTENT

### Supporting Information

Results of macroscopic GISAXS analysis of the tandem nanocrystals fabricated on the Si substrate and the crystalline structures of the tandem nanocrystals. This material is available free of charge via the Internet at <http://pubs.acs.org>.

## AUTHOR INFORMATION

### Corresponding Authors

\*E-mail: hojo.daisuke@wpi-aimr.tohoku.ac.jp. Phone: +81-22-217-6323. Fax: +81-22-217-6323 (D.H.).

\*E-mail: ajiri@tagen.tohoku.ac.jp. Phone: +81-22-217-6321. Fax: +81-22-217-6323 (T.A.).

### Notes

The authors declare no competing financial interests.

## ACKNOWLEDGMENTS

This work was partially supported by a Grant-in-Aid for Young Scientists (A) (No. 23686108) and a Grant-in-Aid for Young Scientists (B) (No. 24760642) from the Ministry of Education, Science, Sports, and Culture (MEXT), Japan. Z.W. thanks the financial support from the Grant-in-Aid for Young Scientists (A) (No. 24686069) from MEXT, Japan, Grant-in-Aid for Scientific Research on Innovative Areas "Nano Informatics" from Japan Society for the Promotion of Science (JSPS), Japan, and National Natural Science Foundation of China (No. 11332013) from China. This work was also supported by the World Premier International Research Center Initiative (WPI) of MEXT, Japan.

## ABBREVIATIONS

NC, nanocrystalline; DHCA, dihydroxyhydrocinnamic acid; RF, radio frequency; FESEM, field-emission scanning electron microscopy; HRTEM, high-resolution transmission electron microscopy; STEM, scanning transmission electron microscopy; GISAXS, grazing-incident small-angle X-ray scattering; XRD, X-ray diffraction; HAADF, high-angle annular dark field

## REFERENCES

- Cardona, M.; Shaklee, K. L.; Pollak, F. H. *Phys. Rev.* **1967**, *154*, 696–720.
- Greenwald, S. *Acta Crystallogr.* **1953**, *6*, 396–398.
- Gray, T. J. *J. Phys. Chem.* **1957**, *61*, 1341–1343.
- Chen, H.-L.; Cheng, H.-C.; Ko, T.-S.; Chuang, S.-Y.; Chu, T.-C. *Jpn. J. Appl. Phys.* **2006**, *45*, 6984–6986.
- Sotiriou, C. A.; Hirt, A. M.; Lozach, P.-Y.; Teleki, A.; Krumeich, F.; Pratsinis, S. E. *Chem. Mater.* **2011**, *23*, 1985–1992.
- Tanaka, A.; Ogino, A.; Iwaki, M.; Hashimoto, K.; Ohnuma, A.; Amano, F.; Ohtani, B.; Kominami, H. *Langmuir* **2012**, *28*, 13105–13111.
- Malassis, L.; Massé, P.; Delapierr, M. T.; Morinet, S.; Weisbecker, P.; Kravets, V.; Grigorenko, A.; Barois, P. *Langmuir* **2013**, *29*, 1551–1561.
- Chen, C.-C.; Tsai, C.-Y.; Ko, F.-H.; Pun, C.-C.; Chen, H.-L.; Chen, P.-H. *Jpn. J. Appl. Phys.* **2004**, *43*, 3843–3848.
- Hamed, M.; Wigenius, J.; Tai, F.-I.; Björk, P.; Aili, D. *Nanoscale* **2010**, *2*, 2058–2061.
- Sakai, N.; Tsuma, T. *Adv. Mater.* **2010**, *22*, 3185–3188.
- Dai, J.; Xu, C. X.; Sun, X. W. *Adv. Mater.* **2011**, *23*, 4115–4119.
- Likovich, E. M.; Jaramillo, R.; Russell, K. J.; Ramanathan, S.; Narayananamurti, V. *Adv. Mater.* **2011**, *23*, 4521–4525.
- Pan, Z.; Zhang, H.; Cheng, K.; Hou, Y.; Hua, J.; Zhong, X. *ACS Nano* **2012**, *6*, 3982–3991.
- Dai, Q.; Chen, J.; Lu, L.; Tang, J.; Wang, W. *Nano Lett.* **2012**, *12*, 4187–4193.
- MacDonald, B. I.; Martucci, A.; Rubanov, S.; Watkins, S. E.; Mulvaney, P.; Jasieniak, J. J. *ACS Nano* **2012**, *6*, 5995–6004.
- Yang, Y.; Córdoba, W. R.; Xiang, X.; Lian, T. *Nano Lett.* **2012**, *12*, 303–309.
- Ibáñez, M.; Zamani, R.; Gorsse, S.; Fan, J.; Ortega, S.; Cadavid, D.; Morante, J. R.; Arbiol, J.; Cabot, A. *ACS Nano* **2013**, *7*, 2573–2586.
- Yu, H.; Chen, M.; Rice, P. M.; Wang, S. X.; White, R. L.; Sun, S. *Nano Lett.* **2005**, *5*, 379–382.
- Sun, X.; Huls, N. F.; Sigdel, A.; Sun, S. *Nano Lett.* **2012**, *12*, 246–251.
- Schladt, T. D.; Graf, T.; Köhler, O.; Bauer, H.; Detzsch, M.; Mertins, J.; Branscheid, R.; Kolb, U.; Tremel, W. *Chem. Mater.* **2012**, *24*, 525–535.
- Yamada, Y.; Tsung, C.-K.; Huang, W.; Huo, Z.; Habas, S. E.; Soejima, T.; Aliaga, C. E.; Somorjai, G. A.; Yang, P. *Nat. Chem.* **2011**, *3*, 372–376.
- Wu, L.; Xing, J.; Hou, Y.; Xiao, F. Y.; Li, Z.; Yang, H. G. *Chem.—Eur. J.* **2013**, *19*, 8393–8396.
- Kuwauchi, Y.; Takeda, S.; Yoshida, H.; Sun, K.; Haruta, M.; Kohno, H. *Nano Lett.* **2013**, *13*, 3073–3077.
- Pu, Y.-C.; Wang, G.; Chang, K.-D.; Ling, Y.; Lin, Y.-K.; Fitzmorris, B. C.; Liu, C.-M.; Lu, X.; Tong, Y.; Zhang, J. Z.; Hsu, Y.-J.; Li, Y. *Nano Lett.* **2013**, *13*, 3817–3817.
- Milijevic, M.; Geiseler, B.; Bergfeldt, T.; Bockstaller, P.; Fruk, L. *Adv. Funct. Mater.* **2014**, *24*, 907–915.
- Li, X.-N.; Yuan, Z.; He, S.-G. *J. Am. Chem. Soc.* **2014**, *136*, 3617–3623.
- Byeon, J. H.; Kim, Y.-W. *ACS Appl. Mater. Interfaces* **2014**, *6*, 763–767.
- Bryant, G. W. *Phys. Rev. B* **1988**, *37*, 8763–8772.
- Chamarro, M.; Gourdon, C.; Lavallard, P. *Phys. Rev. B* **1996**, *53*, 1336–1342.
- Alivisatos, A. P. *Science* **1996**, *271*, 933–937.
- Kwon, K.-W.; Shim, M. *J. Am. Chem. Soc.* **2005**, *127*, 10269–10275.
- Habas, S. E.; Lee, H.; Radmilovic, V.; Somorjai, G. A.; Yang, P. *Nat. Mater.* **2007**, *6*, 692–697.
- Fan, F.-R.; Liu, D.-Y.; Wu, Y.-F.; Duan, S.; Xie, Z.-X.; Jiang, Z.-Y.; Tian, Z.-Q. *J. Am. Chem. Soc.* **2008**, *130*, 6949–6951.
- Park, J.; Zheng, H.; Jun, Y.-W.; Alivisatos, A. P. *J. Am. Chem. Soc.* **2009**, *131*, 13943–13945.
- Fan, F.-R.; Ding, Y.; Liu, D.-Y.; Tian, Z.-Q.; Wang, Z. L. *J. Am. Chem. Soc.* **2009**, *131*, 12036–12037.
- Figueroa, A.; Huis, M. V.; Zanella, M.; Genovese, A.; Marras, S.; Falqui, A.; Zandbergen, H. W.; Cingolani, R.; Manna, L. *Nano Lett.* **2010**, *10*, 3028–3036.

- (37) Wang, W.; Goebl, J.; He, L.; Aloni, S.; Hu, Y.; Zhen, L.; Yin, Y. *J. Am. Chem. Soc.* **2010**, *132*, 17316–17324.
- (38) Wang, D.; Li, Y. *Adv. Mater.* **2011**, *23*, 1044–1060.
- (39) Motl, N. E.; Bondi, J. F.; Schaak, R. E. *Chem. Mater.* **2012**, *24*, 1552–1554.
- (40) Huang, X.; Wang, M.; Willinger, M.-G.; Shao, L.; Su, D. S.; Meng, X.-M. *ACS Nano* **2012**, *6*, 7333–7339.
- (41) Buso, D.; Guglielmi, M.; Martucci, A.; Mattei, G.; Mazzoldi, P.; Sada, C.; Post, M. L. *Cryst. Growth Des.* **2008**, *8*, 744–749.
- (42) Jebril, S.; Kuhlmann, H.; Müler, S.; Ronning, C.; Kienle, L.; Duppel, V.; Mishra, Y. K.; Adelung, R. *Cryst. Growth Des.* **2010**, *10*, 2842–2846.
- (43) Hojo, D.; Togashi, T.; Iwasa, D.; Arita, T.; Minam, K.; Takami, S.; Adschari, T. *Chem. Mater.* **2010**, *22*, 1862–1869.
- (44) Hojo, D.; Togashi, T.; Adschari, T. *Jpn. J. Appl. Phys.* **2013**, *52*, 110113.
- (45) Hitosugi, T.; Ueda, A.; Nakao, S.; Yamada, N.; Furubayashi, Y.; Hirose, Y.; Hasegawa, T. *Appl. Phys. Lett.* **2007**, *90*, 212106.
- (46) Zhang, J.; Ohara, S.; Umetsu, M.; Naka, T.; Hatakeyama, Y.; Adschari, T. *Adv. Mater.* **2007**, *19*, 203–206.
- (47) Kaneko, K.; Inoke, K.; Freitag, B.; Hungria, A. B.; Midgley, P. A.; Hansen, T. W.; Zhang, J.; Ohara, S.; Adschari, T. *Nano Lett.* **2007**, *7*, 421–425.
- (48) Murakami, M.; Matsumoto, Y.; Nakajima, K.; Makino, T.; Segawa, Y.; Chikyow, T.; Ahmet, P.; Kawasaki, M.; Koinuma, H. *Appl. Phys. Lett.* **2001**, *78*, 2664–2666.
- (49) Ho, Y.-T.; Chang, K.-S.; Liu, K.-C.; Hsieh, L.-Z.; Liang, M.-H. *Cryst. Res. Technol.* **2013**, *48*, 308–313.